Impingement heat transfer with pressure recovery

Derwalt J. Erasmus[1,*], Matti Lubkoll[1], Ken J. Craig[2], Theodor W. von Backström[1]

[1] Solar Thermal Energy Research Group (STERG) Department of Mechanical and Mechatronic Engineering, Stellenbosch University, Private Bag X1, Matieland 7602, South Africa

[2] Department of Mechanical and Aeronautical Engineering, University of Pretoria, Pretoria 0002, South Africa

*Correspondence to: Derwalt J. Erasmus. Email: erasmusderwalt@gmail.com

Abstract

A conventional impinging jet is effective at transferring a large heat flux. However a significant pressure loss is also experienced by the free jet of a jet impingement heat transfer device due to rapid expansion because it does not incorporate effective pressure recovery. A novel high-flux impingement heat transfer device, called the Tadpole, is developed to improve the heat transfer and pressure loss (performance) characteristics of the conventional impingement domain by incorporating pressure recovery with a diffuser. The Tadpole is scrutinized through an experimental comparison with a conventional jet impinging on the inner wall of a hemisphere under the turbulent flow regime. The Tadpole demonstrates promising capability by exceeding the performance characteristics of the impinging jet by up to 7.3% for the heat transfer coefficient while reducing the pressure loss by 13%. Multiple dimensional degrees of freedom in the Tadpole's flow domain can be manipulated for an enhanced heat transfer coefficient, a reduced total pressure loss or a favourable combination of both metrics. A Computational Fluid Dynamics (CFD) model is developed, the Four-Equation Transition SST turbulence model demonstrates satisfactory experimental validation with a deviation of < 5% for the heat transfer coefficient and < 23% for the total pressure loss. The Tadpole is a promising heat transfer device for high-flux applications and is recommended for further work incorporating design improvements and multidimensional optimization.

Nomenclature

Variables

A	Area (m^2)
C_p	Static pressure recovery coefficient (-)
d	Diameter (m)
h	Heat transfer coefficient ($W/(m^2K)$)
K	Loss factor (-)
k	Thermal conductivity (W/(m K))
k	Turbulence kinetic energy (m^2/s^2)
l	Length (m)
$\dot{m}$	Mass flow rate (kg/s)
p	Pressure (Pa)
Pr	Prandtl number (-)
$\dot{Q}$	Heat rate (W)
r	Radius (m)
Re	Reynolds number (-)
T	Temperature (°C or K)
TI	Turbulence intensity (-)
V	Velocity (m/s)
y^+	Dimensionless distance from a wall (-)
α	Angle centred at heat transfer surface origin (°)
α	Absorptivity (-)
ε	Emissivity (-)
ε	Turbulence dissipation rate (m^2/s^2)
η	Efficiency (-)
θ	Angle (°)
ξ	Axial Tadpole offset from concentricity (mm)
ρ	Density (kg/m^3)
ϕ	Normalized characteristic (-)
ω	Specific turbulence dissipation rate (1/s)

Subcripts

1	Inlet
2	Outlet
al	Aluminium
aw	Adiabatic wall
c	Nozzle throat
d	Diffuser
DO	Discrete ordinates
es	Exterior heat transfer surface
h	Half angle
i	Inner

is	Interior heat transfer surface
it	Inner tube
n	Nozzle region
nose	Tadpole's nose
os	Outer shell
s	Static
t	Tadpole surface, total

Abbreviations

ABS	Acrylonitrile Butadiene Styrene
CFD	Computational Fluid Dynamics
CSP	Concentrating Solar Power
DO	Discrete Ordinates
HT	Heat Transfer
LES	Large Eddy Simulation
LRN	Low Reynolds Number
HRN	High Reynolds Number
RANS	Reynolds Averaged Navier Stokes
SCRAP	Spiky Central Receiver Air Pre-heater
SS	Supersonic
SST	Shear Stress Transport
TS	Transonic

1 Introduction

Jet impingement heat transfer is an effective heat transfer mechanism capable of absorbing a large heat flux. A typical jet impingement heat transfer device accelerates a fluid flow in a nozzle to emit a free turbulent jet which impacts onto a surface. A stagnation region is formed at the point of impact. From here, the flow is redirected by the impingement surface and becomes a wall jet, transitioning from laminar to turbulent flow. A thin boundary layer develops between the surface and the wall jet. Through this thin boundary layer, a large convective heat transfer coefficient can be achieved.

Various applications exist for an impinging jet in general. This includes paper and glass manufacturing [1], the annealing of metal sheets [2] and electronic microchip cooling [3]. Various applications also exist for a jet impinging within a concave heat transfer surface. For thermal absorption in solar thermal receivers, several concave-surface applications have been explored [4,5,6,7]. Concave-surface impinging jets can also be employed for heating in the de-icing of an aircraft's wing leading edge [8] or compressor's hub [9] as well as for cooling inside a gas turbine blade [10].

Another concave-surface application is a bayonet tube heat exchanger as shown in Fig. 1. In this heat exchanger, heat is transferred between two fluids through multiple bayonet tubes. Within each tube, a fluid enters through an inner tube to proceed towards a concave

3

surface, where it impinges. After impingement, the flow returns through an annulus to exit the heat exchanger. The impingement region plays an important role in the performance of a Bayonet tube [12].
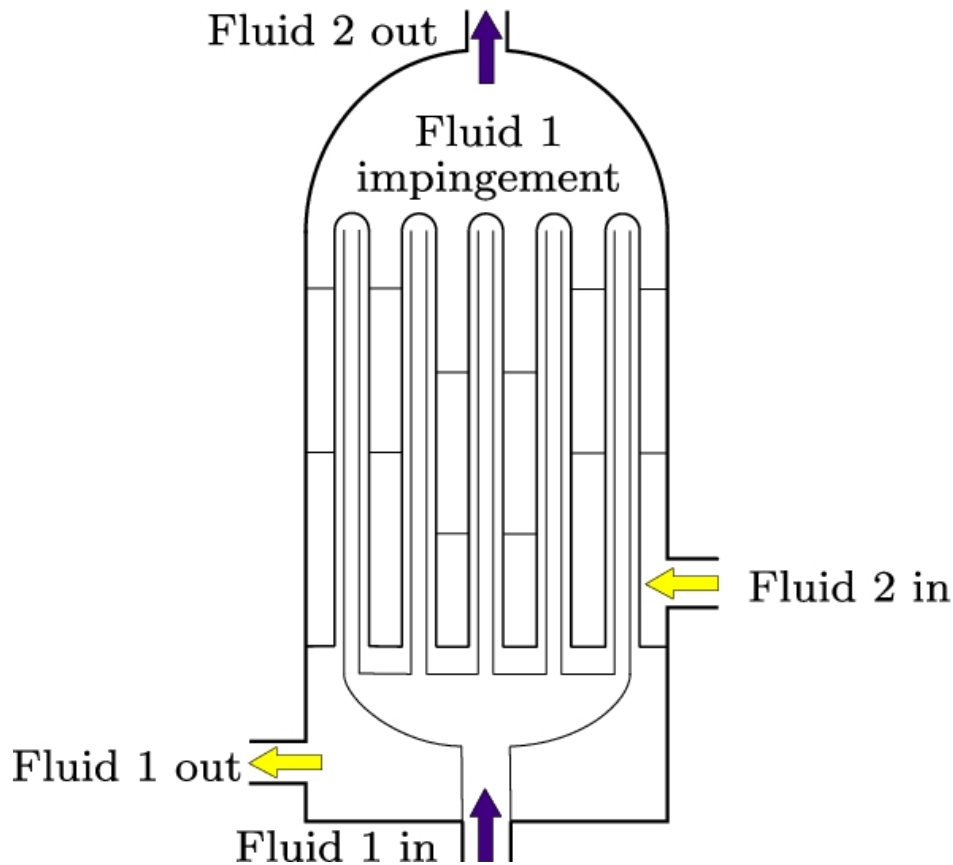

Fig. 1. Bayonet tube heat exchanger (based on [11])

Bayonet tubes have several potential applications, including high-temperature hydrogen production [13] and the steam generators of a nuclear reactor [14]. A multitude of bayonet tubes are also employed in a pressurized air solar thermal receiver called the Spiky Central Receiver Air Pre-Heater (SCRAP) concept [6].

It has been shown that the total pressure loss encountered by an impinging jet can be modelled well with a rapid-expansion loss coefficient [15]. It has been demonstrated that annular diffusers with sufficiently-low expansion angles can reduce total pressure losses from rapid expansion [16, 17]. This indicates that, by incorporating pressure recovery with a diffuser, the conventional impinging jet may be improved.

It has been determined that the impingement heat transfer literature has not explored the incorporation of pressure recovery with an impinging jet, despite an impinging jet typically undergoing a sudden change in flow-area characteristic of rapid expansion. To address this, the present investigation attempts to improve the combination of heat transfer and pressure loss (performance) characteristics in the impingement domain by removing the sudden change in flow area and incorporating pressure recovery. This research is focused on

the development and investigation of the novel Tadpole impingement heat transfer device [18].

2 The Tadpole concept

The Tadpole originated from the observation of the total pressure contoured pathlines of the impinging jet flow domain from a Reynolds Averaged Navier Stokes (RANS) Computational Fluid Dynamics (CFD) simulation. Figure 2 qualitatively illustrates the similarities and differences between the flow domains of the conventional impinging jet and a manifestation of the Tadpole — a key similarity is the impingement region and a key difference is that the Tadpole does not produce a free jet. It is shown that the impinging jet forms large ring vortices around the free jet. These vortices are associated with unfavourable sudden expansion and consequential total pressure losses.

A diffuser can be employed to reduce total pressure losses through enhanced pressure recovery. To recover pressure is to convert dynamic pressure into static pressure [19] and thereby mitigate (permanent) total pressure losses under the turbulent flow regime. The Tadpole was conceived from the idea of replacing the ring vortices around the conventional impinging jet with a device (or a baffle) formed by the vortex boundary shown on the left of Fig. 2. The device in this region avoids a sudden change in flow area by incorporating a diffuser for pressure recovery; and is thereby expected to improve the performance characteristics of the domain. The Tadpole bears similarity to a Venturi volumetric flow meter [20]. A Venturi flow meter contains a nozzle, a throat and a diffuser to accelerate and decelerate a flow while undergoing a relatively low pressure loss without sudden area changes encountered by an orifice plate flow meter, for example.
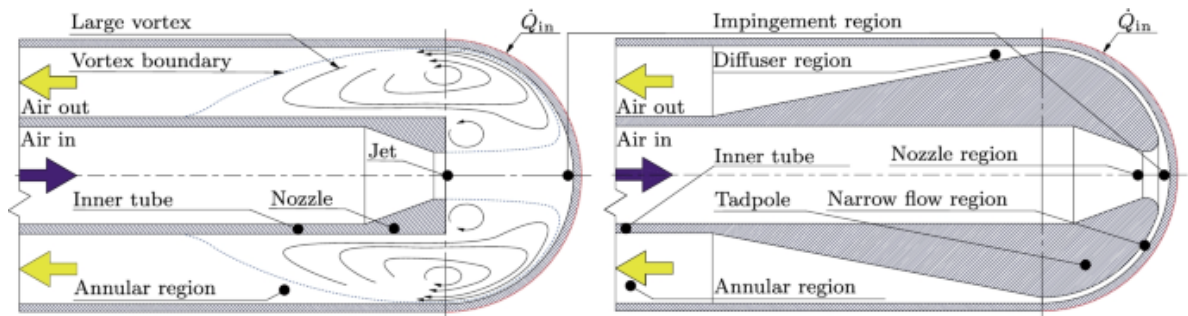

**Fig. 2.** Illustrations of the jet (left) and Tadpole (right) flow domains

In the Tadpole's domain described by Fig. 2, the flow enters through the inner tube to be accelerated in the nozzle region — the dynamic pressure is increased here. The flow subsequently impinges on the interior of a concave surface as the flow direction changes. The flow is then constrained to the narrow flow region, which starts at the Tadpole's nose, reaching a maximum Reynolds number here.

The elevated Reynolds number ensures a thin boundary layer and a large convective heat transfer coefficient on the interior heat transfer surface. In the diffuser region, the flow is expanded to recover the previously developed dynamic pressure into static pressure. The flow subsequently leaves the domain through an annular flow region. The Tadpole's name comes from the shape it displaces in the axisymmetric flow domain as illustrated in Fig. 3.

An example application of the Tadpole within a spike of the SCRAP solar receiver is shown in Fig. 4.
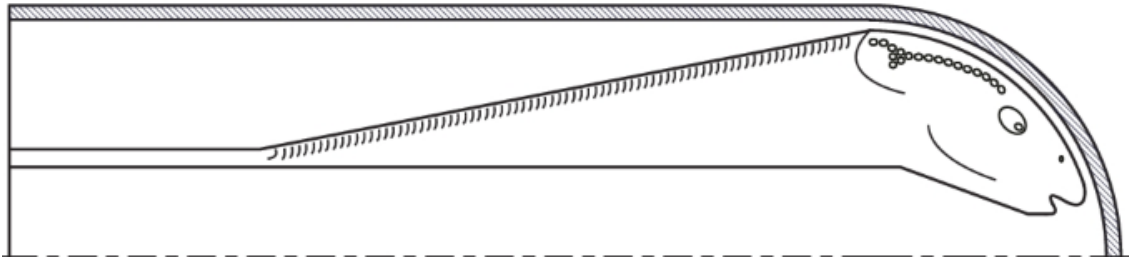
Fig. 3. Axisymmetric illustration demonstrating the origin of the Tadpole. Reproduced from [Erasmus, D.J., Lubkoll, M., Craig, K.J., Von Backström, T.W. Capability of a novel impingement heat transfer device for application in future solar thermal receivers, in: AIP Conference Proceedings, SolarPACES 2019, Vol. 2303, No. 030014. DOI:10.1063/5.0029156.], with the permission of AIP Publishing
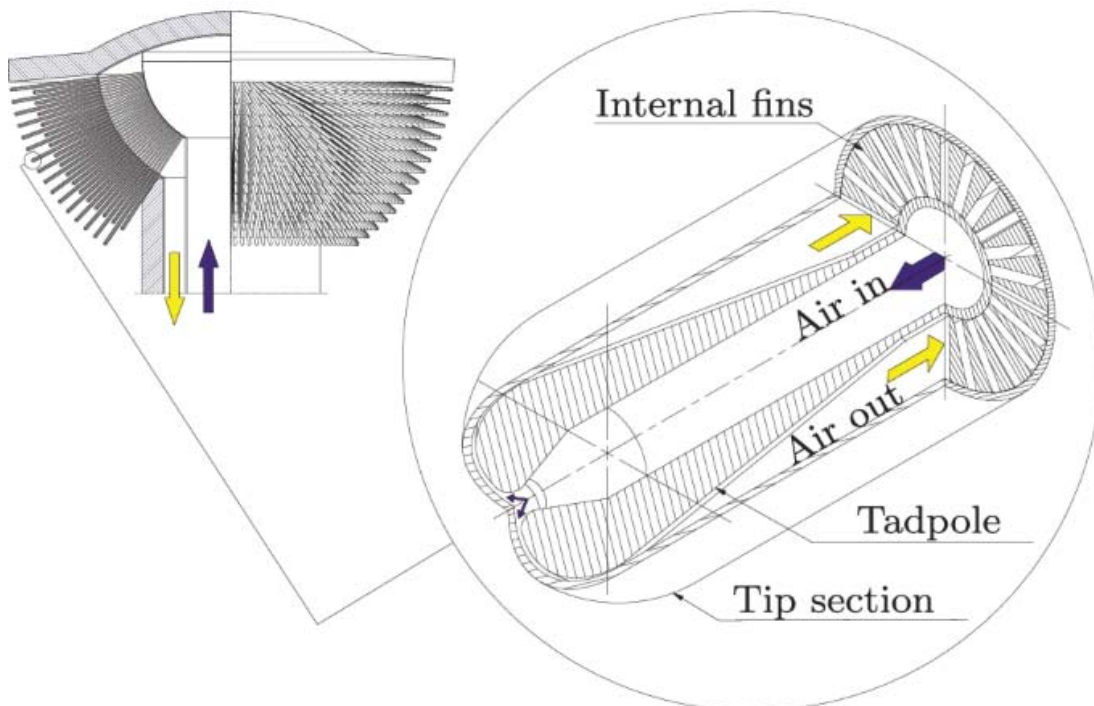
Fig. 4. Implementation of the Tadpole within the SCRAP concept (adapted from [21])

The axial-type impinging receiver from [5] is similar to the Tadpole. Although the flow through the axial-type absorber appears to undergo rapid expansion (with flow separation) through two 45 ° ducts, as well as immediately downstream of the impingement region as shown in the CFD results of [5]. The design does, however, have the benefit of being manufacturable from welded sheet metal.

3 Layout of paper

For its application within the SCRAP concept as well as the impingement domain in general, the Tadpole is investigated here. The Tadpole's flow domain is explored experimentally and by using CFD. Further, it is determined whether the Tadpole is capable of improving the

heat transfer and pressure loss characteristics of the impingement domain in comparison to a conventional jet impinging on a concave surface.

The experimental apparatus and the prototypes are detailed in Sect. 4. The CFD model is described in Sect. 5. An uncertainty analysis is detailed in Sect. 6. Thereafter, the heat transfer and pressure loss experimental results are presented in Sect. 7.1, followed by the validation of the CFD model in Sect. 7.2.

4 Experimental apparatus

4.1 Overview

The experimental apparatus was built by Lubkoll et al. [6] and was modified to investigate jet impingement heat transfer in Erasmus et al. [15]. The setup has been further developed to investigate the heat transfer and pressure loss characteristics of Tadpole prototypes under the turbulent flow regime. The working fluid of the setup is pressurized air supplied by a 10 bar air-supply system. Heat is supplied to the air stream using a steam bath with steam condensation at atmospheric pressure (nominally 100 °C). The reader is referred to Erasmus et al. [15] for a more detailed description of the experimental apparatus and the experimental Tadpole configurations. A similar heat transfer apparatus, making use of condensing-steam heat addition, has been developed by [22].

The heat transfer region of the test section is shown in Fig. 5. A flange around the hemispherical dome interfaces with the steam bath and is sealed using a high-temperature silicone adhesive. Heat is conducted from the exterior heat transfer surface towards the interior heat transfer surface and through the flange before it reaches the convection domain. This combined interaction of conductive and convective heat transfer is termed conjugate heat transfer.

It is shown in Sect. 7.2.3 that the region where most of the heat is transferred into the convection domain is through the dome and the neighbouring flange. For this reason, the conventional area for estimating the average heat flux represents a combination of the hemispherical area and a part of the flange (denoted by the red line in Fig. 5).
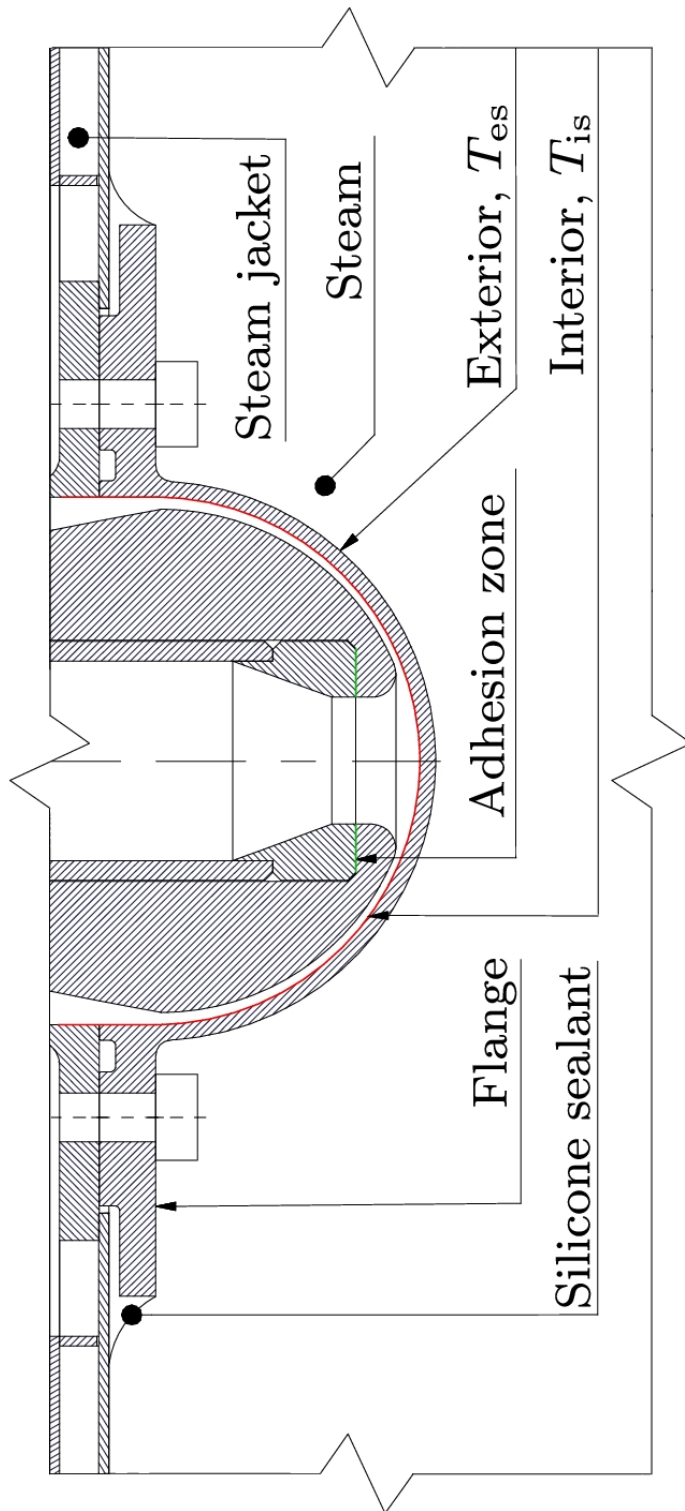
Fig. 5. Sectioned view of heat transfer region

The heat transfer characteristics of an impinging jet or a Tadpole are determined using a combination of T-type thermocouples. The area-weighted-average (overall) heat transfer coefficient over the interior heat transfer surface is determined using the apparatus following the same convention as an impinging jet from the VDI Heat Atlas [23]:

8

$$h_{\mathrm{is}} = \frac{\dot{Q}_{\mathrm{air}}}{A_{\mathrm{is}}(T_{\mathrm{is}} - T_{\mathrm{in}})},$$

(1)

where A_{is} represents the area of the interior heat transfer surface (illustrated as the red line in Fig. 5) and T_{in} is the air flow temperature prior to impingement.

The air mass flow rate is controlled by varying the inlet static pressure with a control valve. An orifice plate is used to determine the mass flow rate. A gauge pressure sensor (Firstrate FST800-10B) and various differential pressure transducers (Freescale MPX2050DP) are used to determine the static pressure and density (from the ideal gas law) upstream and downstream of the Tadpole or impinging jet. The dynamic pressures in these regions are determined using the conservation of mass. This is required to obtain the total pressure loss (Δp_{t}) through the domain.

4.2 Manufacturing

The test section components, with the exception of the Tadpole prototypes and the steam bath, were manufactured from aluminium. The steam bath was manufactured from stainless steel. Figure 5 shows that an experimental Tadpole configuration is made of two components: a nozzle assembly and an attached bulbous plastic part joined by an adhesion contact zone (denoted by the green lines). The main part of the Tadpole is manufactured from hard ABS+ plastic. The material properties are given in Table 1.

The plastic parts of the prototypes were manufactured by 3D-printing. The parts have a solid outer shell made up from 10 layers of 0.12 mm-thick printing filament. Encapsulated by the outer shell, the prototypes are porous inside with a porosity of 50%. The low associated thermal conductivity is chosen because heat transfer through the Tadpole is not desired – this is later investigated with the CFD model in Sect. 7.2. Each part was lightly machined to produce a smooth external surface-finish.

Table 1. Material properties

Material	k $[\frac{\mathrm{W}}{\mathrm{m\,K}}]$	ε [-]	α [-]
ABS, (50% porosity)	0.08176,[1]	0.95,[2]	0.95,[4]
Aluminium 7075-T6 (26 °C)	128,[3]	0.095,[2]	0.095,[4]

[1] Estimated using the porous material conductivity relation from [24] and data from [25]
[2] Mikron Instrument Company [26]
[3] Fives North American Combustion [27]
[4] Kirchhoff's law of thermal equilibrium was assume

4.3 Prototype configurations

4.3.1 Dimensions

The Tadpole's reference flow domain is established in terms of several dimensions in Fig. 6. The prototypes were designed to experimentally investigate the behaviour of the Tadpole's flow domain through a wide variety of characteristic dimensions. The combination of these dimensions are too numerous to investigate in isolation, therefore a prototype-based experimental approach was followed. Several prototype configurations are developed to span a range of key dimensions.

To describe the dimensions required to manufacture and configure the experimental prototypes, Table 2 depicts dimensions applicable to all Tadpole prototype configurations and Table 3 depicts dimensions specific to each prototype configuration.
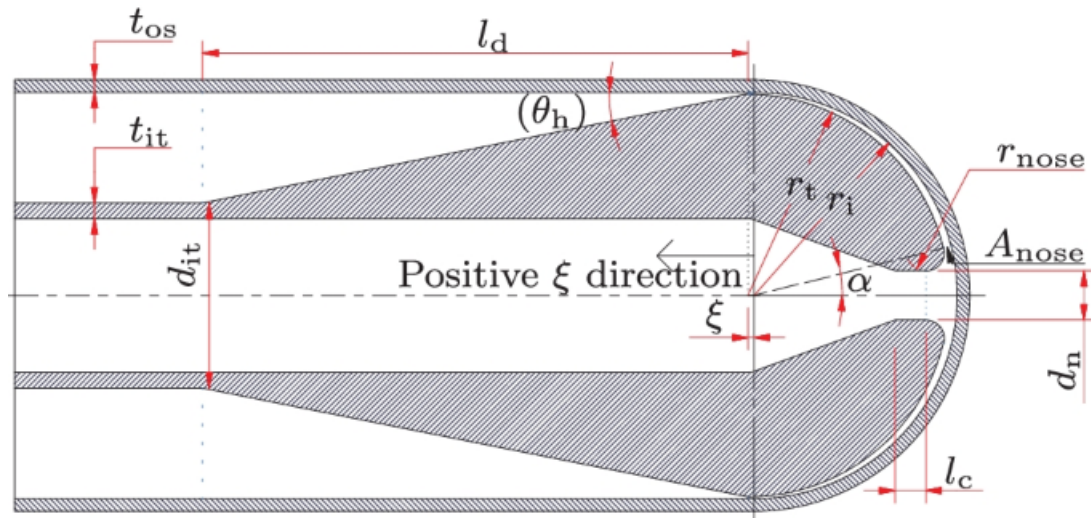

Fig. 6. Physical dimensions of a generic Tadpole — demonstrated in a positive ξ position

Table 2. Dimensions applicable to all Tadpole prototypes (as depicted in Fig. 6**)**

r_i	t_{os}	d_{it}	t_{it}	l_c
[mm]	[mm]	[mm]	[mm]	[mm]
33	2	30	2	5

Table 3. Dimensions of the experimental Tadpole prototype configurations (dimensions depicted in Fig. 6)

Dimension	Unit	16-A	16-B	12-A,ss	12-B	12-C,ts	8-A,ss	8-B
d_n	[mm]	15.8	15.8	11.7	11.7	11.7	7.7	7.7
r_{nose}	[mm]	3	3	2.5	2.5	2.5	2	2
r_t	[mm]	31.3	31.3	32	32	32	32.5	32.5
l_d	[mm]	85	85	90	90	90	95	95
ξ_{low}	[mm]	-1.09	0.263	-0.743	0.157	-0.293	0.0902	1.09
ξ_{high}	[mm]	-0.587	0.663	-0.643	1.16	0.357	0.0902	1.29

4.3.2 Key design decisions

From a prior CFD analysis, it was found that, if the flow velocity reaches a maximum at the Tadpole's nose (depicted at A_{nose} in Fig. 6), separation is avoided near the stagnation region — this is intuitive because with this constraint, a positive pressure gradient is maintained upstream of the Tadpole's nose. This was identified to produce a low total pressure loss in this region. A peak velocity at the Tadpole's nose is therefore the primary design objective. The key dimensions affecting this are the nozzle-region diameter (d_n) and the axial position (ξ).

The secondary objective is to produce a gradual velocity development through the domain to avoid sudden expansion or contraction of the flow. After the primary objective is achieved, the remainder of the dimensions are chosen together to achieve the secondary objective. They are chosen together because they are dependent on each other. In order to predict the kinematic characteristics of the flow domain and chose appropriate dimensions before experimental testing, a kinematic model was developed to estimate the development of the Mach number along an estimated mean pathline, this can be found in Erasmus [28].

4.3.3 Naming convention

The naming convention for the prototypes and configurations in Table 3 are intuitively described using the most significant variables. Here, a prototype refers to a specific physical Tadpole and a configuration refers to an axial position of the physical prototype. Each physical prototype is named with a number according to its nozzle diameter and the configuration of each prototype is named according to its relative axial position (ξ), such as 8-A or 8-B for example. With A depicting the prototype configuration where the nose is nearest to the interior heat transfer surface (lesser ξ) and B depicting the farthest (greater ξ). There is also a special-case configuration, 12-C, with an axial position between the 12-A and 12-B configurations.

4.3.4 Diffuser design

Diffusers cause higher total pressure losses than nozzles with similar lengths and area ratios because diffusers operate with an adverse pressure gradient. The adverse pressure gradient permits the flow to separate from the walls and cause a stall. The diffuser of the Tadpole is most appropriately classified as an 'annular diffuser' with a 'constant diameter outer wall' and a 'conical centerbody', where similar diffusers were investigated by Adkins et al. [17]. The Tadpole's diffuser differs from this classification only because the outlet of the diffuser is an annulus whereas in the work of Adkins et al. [17] the outlet is an open circular pipe.

The performance of a diffuser can be characterized by the pressure loss coefficient [29]. A higher loss coefficient indicates a less efficient diffuser. The lost total pressure ($p_{t,1}-p_{t,2}$) is normalized with the diffuser's inlet dynamic pressure to obtain the diffuser total pressure loss coefficient:

$$K_d = \frac{p_{t,1} - p_{t,2}}{\frac{1}{2}\rho V_n^2}.$$

(2)

In this study, $p_{t,1}$ and $p_{t,2}$ correspond with total-pressure measuring points at the inlet and at the outlet of the domain, respectively (see Fig. 4 and Fig. 7); thereby also including the less-significant nozzle and pipe losses to enable a comparison with the previously-investigated impinging jets.

The diffuser performance can also be expressed as an efficiency in terms of the inlet and outlet static pressures and the inlet velocity [30]:

$$\eta_d = \frac{p_{s,2} - p_{s,1}}{\frac{1}{2}\rho V_1^2 (1 - (\frac{A1}{A2})^2)}.$$

(3)

Kröger [29] showed that, for a round conical diffuser, the maximum achievable efficiency is around 90% with an expansion half angle of 4.3 ° and a range of area ratios between 2 and 9. It is also noted that, with increasing expansion half angles, the sensitivity of the diffuser efficiency to the diffuser area ratio increases with larger area ratios resulting in lower efficiencies. A further observation is that half angles below 4 ° do not result in an increase in the diffuser efficiency because of an increase in skin-friction drag. The rate of increase in drag from reducing the half angle below the optimum value is not significant in comparison to increasing the angle. This is a key finding because it demonstrates that a favourable diffuser can still have a smaller than optimal expansion angle.

Adkins et al. [17] experimentally found that their smallest-tested cone half angle of 12.5 ° achieved a C_p of 0.6. This corresponds to an efficiency (η_d) of up to 91% (for an area ratio of 1.489). This demonstrates that a similar maximum diffuser efficiency of a round conical diffuser is achievable. Johnston [30] obtained experimental results for a diverging annular diffuser and achieved efficiencies of 85% with a diffuser angle of 6.5 °.

4.3.5 Design constraints

In the present work, the diffuser half angles, Θ_h, were constrained between 11 ° and 13 ° for all cases. The apparatus did not permit longer diffusers than these — longer diffusers (around 7 °) would have been chosen if permitted.

In Erasmus et al. [15], impinging jet nozzle assemblies including nozzle diameters of d_n=16mm and d_n=12mm were tested to explore a low and high nozzle-outlet Reynolds number. An important dimensional constraint is for the nozzle region of two Tadpoles to be comparable to these two jets with a similar nozzle-region diameter. These nozzle assemblies are physically part of the Tadpole prototypes as shown in Fig. 5. A Tadpole with d_n=8mm was also created to explore even higher velocities — this makes up three different Tadpole prototypes. The imposed constraints were that the Tadpole's radius (r_t), its nose radius (r_{nose}) and its axial position (ξ) be selected in order to satisfy the above-mentioned primary and secondary objectives.

The nozzle region convergence angle was constrained at 20 ° as in Erasmus et al. [15] because it was found to have a small loss coefficient [16] and it enables comparability to the previous impinging jets.

The prototypes are well supported around the circumference with the stiff support of the inner tube. Although, due to the small dimension of the narrow flow region, possible oscillations of the prototypes around the axis have been identified as a possible concern at the start of the exploration. For the the first-developed 16-mm prototype with larger tolerances, such oscillations were deemed negligible from operational experience. On the later-developed prototypes with finer tolerances: the 12-mm and 8-mm prototypes, it was desired to eliminate the possibility of such oscillations, and so small locating fins were added downstream of the narrow flow region around 120 ° intervals to precisely constrain concentricity between the Tadpole and the surrounding outer shell. In a future high-temperature/on-sun application, such locating fins can be implemented to constrain the domain and differential thermal expansion. The Tadpole and the heat transfer shell can also be manufactured together as a single, bonded structure (interfacing with fins) by 3D printing.

4.3.6 Supersonic exploration

The area development of the Tadpole's flow domain characteristically converges before diverging. This means that if a large-enough pressure difference over the domain is applied, then N_{Mach}=1 is reached at the Tadpole's nose (nominally the minimum flow area region) and the diverging flow area downstream of the nose further accelerates the flow into the supersonic realm. For the coincidental inherent capability of the Tadpole to reach supersonic speeds, the heat transfer and pressure loss characteristics in this realm is also explored experimentally. The prototype configurations in Table 3 that venture into the transonic and supersonic realms are denoted with the abbreviations: ts and ss respectively.

4.3.7 Axial thrust considerations

During experimental operation, it was found that the Tadpole generates thrust in the axial direction. The thrust is generated by the pressure and shear stresses acting on the exposed surfaces of the Tadpole (from the nozzle region to the diffuser). The thrust causes the relative axial distance between the Tadpole and the interior heat transfer surface centre points (ξ) to increase slightly with an increase in the air mass flow rate. Moreover, the apparatus elastically deforms during a test in relation to mass flow rate.

To address this characteristic, the axial positions were measured at a low mass flow rate (to determine ξ_{low}) and at a high mass flow rate (to determine ξ_{high}) of a varying mass flow rate test as shown in Table 3. These ξ values were linearly interpolated for other data-points based on the mass flow rate to estimate the geometry of the flow domain. For the CFD model developed in Sect. 5, interpolated ξ values are used for the mesh of each simulated mass flow rate.

4.4 Experimental procedure

The full experimental procedure incorporates a test at ambient temperature (unheated) and a heat transfer test with the steam-system activated. The unheated test determines the total pressure loss characteristics of the domain without the influence of air flow temperature changes. The experimental measurements are time-averaged over approximately 6 min for the unheated tests and 10 min for the heated tests after steady-state operation is reached. The time-averaging accounts for minor fluctuations of the air-supply temperature due to the air-supply system being situated outside the laboratory; as well as to eliminate effects of instabilities such as vibration.

5 CFD modelling

This section describes the development of a CFD model using ANSYS Fluent® which enables predicting an extensive variety of applications and operating conditions of the Tadpole's flow domain.

5.1 Turbulence modelling

To model a turbulent heat transfer flow domain, the compressible Navier Stokes equations can be employed and solved computationally with turbulence modelling. Turbulent flow can be modelled by making use of variable viscosity models to emulate the dissipative nature of turbulence. An appropriate viscous RANS turbulence model is required for the Tadpole's CFD model. It is required to model an impingement region near the nose of the Tadpole and an adverse pressure gradient in the diffuser.

Two kinds of RANS turbulence models exist, High Reynolds Number (HRN) turbulence models and Low Reynolds Number (LRN) models. HRN models estimate the near-wall boundary layer characteristics with a simplified theoretical function in the first computational node, the most commonly used HRN model is the standard k-ε model by Launder and Spalding [31]. Contrarily, LRN models resolve the boundary layer in more detail computationally. The first computational node is placed well within the viscous sub-layer (near-wall region) of the boundary layer — around the vicinity of $y^+\approx1$ or less [32]. LRN turbulence models are more accurate than HRN models but are more computationally expensive to use [33].

McDougall [34] investigated the implementation of jet impingement heat transfer on the SCRAP concept by developing a 2D (axisymmetric) RANS CFD analysis. McDougall considered HRN models (including the k-ε model) and various LRN models. He found that the k-ω Shear Stress Transport (SST) LRN turbulence model by Menter [35], with the extension of an intermittency function and a production of k limiter, correlated well with the heat transfer experimental results from Lee et al. [36], performed better than the HRN models and performed marginally better than the Transition SST LRN turbulence model by Langtry and Menter [37].

Craig et al. [38] investigated a similar domain using an axisymmetric RANS CFD model with the Four-Equation Transition SST turbulence model and a 3D Large Eddy Simulation (LES)

CFD model. The LES model as well as the axisymmetric RANS model were validated by the experimental results from Lee et al. [36]. Zuckerman and Lior [39] observed that the v^2f model, the k-ω model and the SST model demonstrated good validation for an impinging jet relative to the k-ε model.

Erasmus et al. [15] validated both the k-ω SST and the Four-Equation Transition SST-based CFD models for a concave hemispherical surface with a focus on both the heat transfer and pressure loss characteristics.

The k-ω SST and Transition SST RANS turbulence models are therefore both suitable for application in the impingement domain. These models are investigated further in the following section. A brief overview of these models and their features now follows.

The k-ω SST model combines the k-ε model in the free stream region and the k-ω model near the wall with a blending function. The benefit of this model is that it is not sensitive to turbulence boundary conditions which is an issue of the k-ε model. This characteristic is important and necessary for this domain because the turbulence intensity boundary conditions represent an uncertainty [40]. The SST model is also suitable to model an adverse pressure gradient [32] — a requirement for the Tadpole.

The impingement region of an impinging jet typically contains a stagnation region and a subsequent laminar to turbulent transition [38]. Intermittency is a turbulence metric used to quantify the fraction of time that a flow at a localized region is turbulent (as opposed to laminar) and it is used to describe flow that is transitional [40]. An intermittency function can also be included alongside the k-ω SST model in FLUENT® to improve the modelling quality of transitional flows.

In some cases — such as near a stagnation region — the turbulence model over-approximates the turbulence kinetic energy, k. The production of k limiter mitigates this effect [34].

The k-ω SST model was the basis for the development of the Four-Equation Transition SST model. This model couples the former model along with functions describing intermittency and a criterion for the transition of the flow between laminar and turbulent [32]. The model has been developed for domains that contain regions of transitional flow, as in the present application.

5.2 Model development

Within the experimental apparatus, heat travels from steam, through an aluminium volume and a flange to reach the air stream. Because steam condenses at a constant temperature, the heat source is modelled using a constant temperature boundary condition. The flow domain is axisymmetric.

In order to integrate the conjugate heat transfer characteristics in the domain, a bottom-up modelling approach is taken for the model development. All significant parts within the validation domain are therefore modelled. This includes the aluminium nozzle assembly, the

annulus, flanges as well as the plastic ABS+ parts of the Tadpole prototypes. The CFD flow domain is illustrated in Fig. 7.
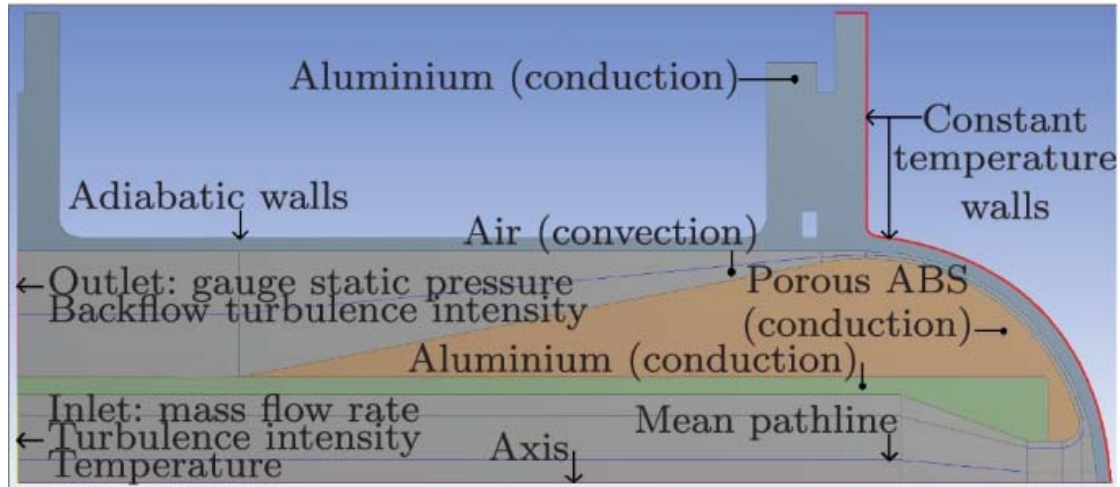

Fig. 7. Flow domain of the Tadpole's experimental validation CFD model

Three data-points from each configuration of the heated system experimental results were chosen for validation. Moreover, the first data-point, the nearest to middle and the last data-point of the investigated heat transfer coefficients. Because the geometry of the experimental flow domain changes during each test (previously detailed in Sect. 4.3.7), the geometry at each validation point mass flow rate was recreated (15 unique geometries).

Although the supersonic characteristics of the flow domain were investigated experimentally, the supersonic realm is not validated using the CFD model because the Tadpole's envisaged application is not supersonic.

5.3 Boundary conditions

As depicted in Fig. 7, the experimental validation boundary conditions are:

- The inlet temperature, mass flow rate and turbulence intensity[1] (mass flow rate inlet).
- The outlet gauge static pressure and backflow turbulence intensity (pressure outlet).
- The temperature of the exterior heat transfer surface (constant temperature).
- Adiabatic conditions on all other exterior surfaces (zero heat flux).

Table 4 gives the set of boundary conditions for the validation CFD simulations. The ξ

values for the simulation states were interpolated or extrapolated based on the mass flow rate and the ξ_{low} and ξ_{high} values from the unheated tests (as detailed in Sect. 4.3.7). Experiments were conducted at $p_{abs,atm}$=101.35kPa.

Table 4. Boundary conditions and variables for the CFD Tadpole validation simulations

State	Unit	16-A	16-B	12-B	12-C,ts	8-B
State 1						
$\dot{m}_{in}$	$[\frac{kg}{s}]$	0.0151	0.0136	0.0163	0.0161	0.0117
T_{in}	[°C]	28.39	31.84	18.40	24.83	21.28
T_{es}	[°C]	98.68	98.84	97.90	97.94	97.99
$P_{g,out}$	[kPa]	54.18	48.91	55.36	57.45	35.37
TI_{in}	[%]	4.244	4.300	4.205	4.210	4.381
TI_{out}	[%]	5.021	5.087	4.975	4.981	5.184
ξ	[mm]	-0.390,[2]	0.305	0.184	0.03,[2]	1.12
State 2						
$\dot{m}_{in}$	$[\frac{kg}{s}]$	0.0444	0.0596	0.0600	0.0442	0.0193
T_{in}	[°C]	27.18	32.01	18.30	26.02	21.68
T_{es}	[°C]	96.17	95.94	93.36	94.86	96.76
$P_{g,out}$	[kPa]	218.1	309.0	302.4	215.4	73.27
TI_{in}	[%]	3.709	3.575	3.573	3.711	4.118
TI_{out}	[%]	4.389	4.230	4.227	4.391	4.872
ξ	[mm]	-0.43,[2]	0.460	0.588	0.174,[2]	1.17
State 3						
$\dot{m}_{in}$	$[\frac{kg}{s}]$	0.0865	0.120	0.117	0.0921	0.0326
T_{in}	[°C]	26.09	35.58	22.21	25.59	23.47
T_{es}	[°C]	93.30	93.26	89.10	90.94	94.87
$P_{g,out}$	[kPa]	465.0	657.4	633.5	493.2	148.7
TI_{in}	[%]	3.413	3.276	3.287	3.386	3.855
TI_{out}	[%]	4.038	3.876	3.889	4.006	4.561
ξ	[mm]	-0.589	0.664	1.12	0.342	1.27

[2] This value corresponds to the corrected CFD result

5.4 Modelling considerations

5.4.1 Turbulence and viscous effects

Section 5.1 revealed two RANS turbulence models that are most suitable for this flow domain: the k-ω SST model and the Four-Equation Transition SST model. These models are both considered.

Both models were implemented with the production of k limiter and the Kato-Launder model. The k-ω SST model was additionally used with the intermittency transition extension function, turbulence compressibility as well as low Reynolds number correction. It was found that the solver often diverges without low Reynolds number correction. This correction equation is understood to improve the modelling of the laminar flow region near the stagnation region.

The energy transport equation must be solved to account for the flow of heat through the domain as well as viscous heating. Compressibility effects are accounted for because the flow may venture near sonic velocity.

5.4.2 Radiation

The Tadpole's exterior surface is characteristically near the interior heat transfer surface. The view factor between the two surfaces is almost unity — for example, the 12-A configuration's view factor is 0.98. This means that, if the Tadpole's surface is colder than the temperature of the heat transfer surface, there is net radiative heat transfer to the Tadpole's surface. This heat accordingly moves into the air flow. This effect may especially be pertinent at elevated operating temperatures according to the fourth temperature exponent in the Stefan-Boltzmann law equation.

The radiation between surfaces enclosing the convection flow domain is modelled with the discrete ordinates (DO) radiation model. This model is appropriate for localized heat sources and has a modest solving computational requirement [32]. Because the narrow flow region is thin and free of particles, the participation of air in radiation modelling was neglected.

5.4.3 Discretization and solver settings

The default discretization resolution for the dicrete ordinates (DO) radiation model was used because the results were found to be robust to refinement from the default settings. Moreover, for both Θ_{DO} and ϕ_{DO}, 2 divisions and 1 pixel were chosen.

The Coupled pressure-velocity solver scheme was found to be robust and versatile for this domain. For spatial discretization: Green-Gauss node-based was used for the gradients; second-order was used for pressure; second-order Upwind was used for the energy equation, density, momentum, turbulence kinetic energy and turbulence dissipation rate; finally, the first-order Upwind scheme was used for intermittency and the discrete ordinates model.

It was found that the solver often diverges without high-order-term relaxation as the second-order terms in the transport equations may render the solver unstable. The second-order terms were opted for here for improved numerical accuracy. The default relaxation parameters suggested by Fluent® worked satisfactorily. Moreover, the pressure and momentum equations were relaxed with a factor of 0.5 while for energy and density, 1 was used.

5.4.4 Mesh generation

An example mesh is shown in Fig. 8. The convection flow domain was partitioned (as shown in Fig. 7) so that a fully-structured mesh could be generated. The structured grid enables resolving fine detail within the domain as well as robust grid independence. The convection structured mesh scales for all prototype configurations. A high resolution is not required within the conduction domain (solid materials) because conduction temperature gradients are linear in these regions so it was resolved by quadrilaterals with a minimum face size of 0.6 mm.
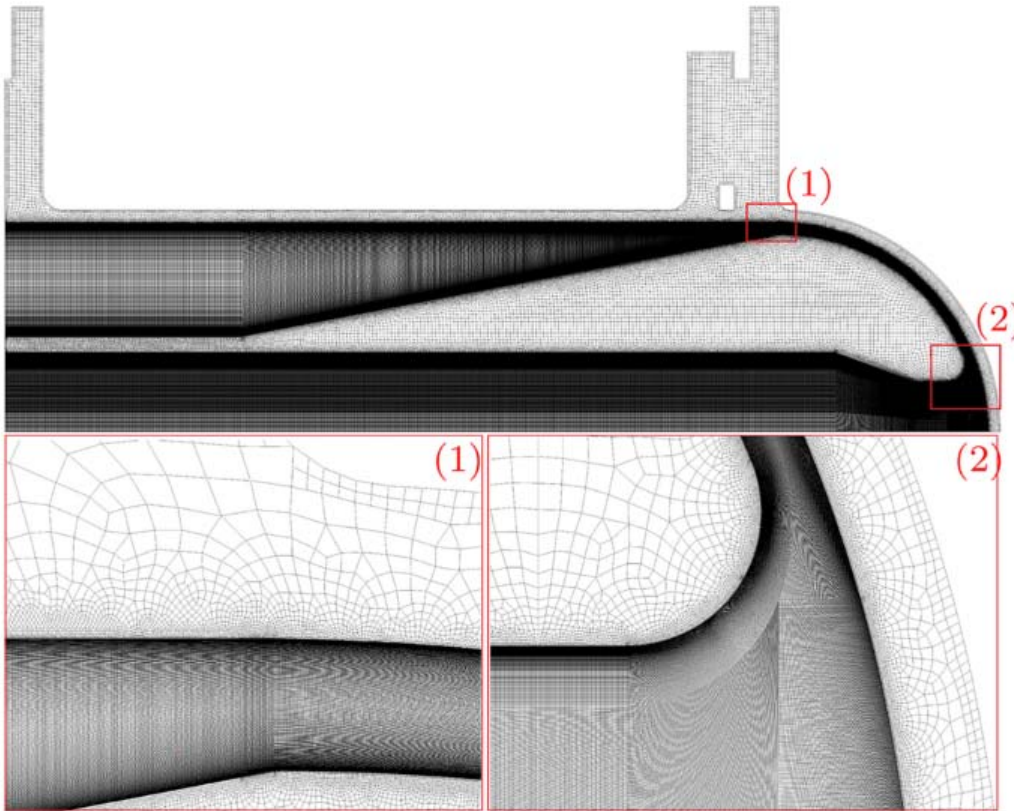
Fig. 8. Computational mesh with enlarged sections – left (1) and right (2) – of a typical axisymmetric case, mesh node count: 1.8×106

5.4.5 Grid independence

A grid independence study was conducted for the validation mesh with the largest cell size for the structured mesh region (convection domain) — the 16-B mesh and the boundary conditions used correspond with the largest experimental validation mass flow rate and the largest anticipated y^+ value. The grid dependence results are shown in Fig. 9.

It is demonstrated that the heat transfer coefficient and the total pressure loss converge at 0.25% and 0.58% respectively between the two most fine meshes. This is sufficient because it is well below the experimental uncertainty. The mesh with around 1.8×10^6 nodes is the chosen mesh. In the narrow flow region, there are 120 divisions perpendicular to the flow direction and 1000 divisions parallel to the flow direction. For the LRN turbulence models, the wall condition of $y^+\approx1$ [33] was achieved for all simulations after additional near-wall refinement in some meshes.
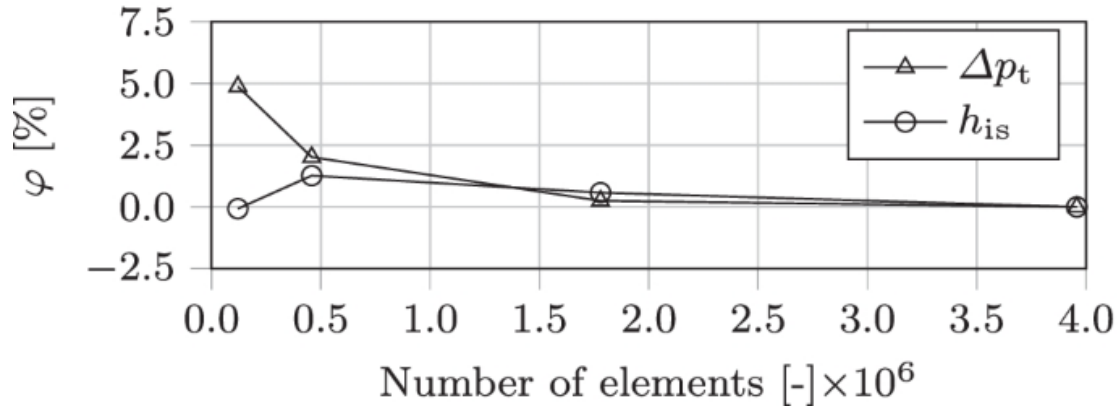
Fig. 9. Deviation of the performance characteristics from that of the finest computational mesh over the number of elements in the mesh

6 Uncertainty

6.1 Experimental sensor uncertainty

The propagation of the calibration uncertainty of sensor measurements is estimated on the key operating characteristics according to the methodology of Taylor [41]. The results of the analysis are given in Table 5. The sensor uncertainty affects all tests and thus it is understood that a relative comparison between Tadpole prototype configurations and impinging jets are reliable. The comparison with CFD results are subject to error bars reflecting this uncertainty.

Table 5. Experimental uncertainty propagation

Uncertainty	Unit	h_{is}	$\dot{m}_{air}$	Re_n	ΔP_t	K_{loss}
Maximum	[%]	6.43	2.74	2.74	7.42	9.68
Mean	[%]	2.91	0.146	0.146	0.522	0.699

6.2 Geometric uncertainty

It must be noted that a dominating uncertainty for re-creating the flow domain is expected to be the axial position measurement (ξ) of 0.5 mm. This is the discretization of the axial position measurement device. The ξ measurement has a significant effect on the flow area at the Tadpole's nose. The effect on a particularly sensitive Tadpole configuration is an uncertainty of around 32% on the minimum flow area (at the Tadpole's nose). This is expected to affect the heat transfer and pressure loss characteristics significantly. It is for this reason that the effect of other minor (and not practically quantifiable) prototype geometric imperfections on the performance characteristics are not scrutinized. Such imperfections include the previously described Tadpole's surface finish, the positioning fins, concentricity and pressure-related elastic deformation of the Tadpole. A sensitivity analysis is conducted in Sect. 7.2.2 on the ξ measurement to understand its effect on the CFD validation together with a correction of the most affected results.

7 Results

This section firstly presents the experimental heat transfer and pressure loss characteristics of the Tadpole prototype configurations in perspective with the impinging jets from Erasmus et al. [15] (denoted as 12-jet and 16-jet). Thereafter, the CFD model is validated with the experimental results and further insight is gleaned from the CFD model.

## 7.1 Experimental results

7.1.1 Heat transfer characteristics

The overall heat transfer coefficients for the Tadpole configurations as well as the impinging jets are presented in Fig. 10. The coefficients develop almost linearly with mass flow rate. The heat transfer coefficients of the Tadpole configurations straddle the impinging jets with corresponding nozzle diameters. The two supersonic cases represent the highest heat transfer coefficients with the steepest gradients as well.
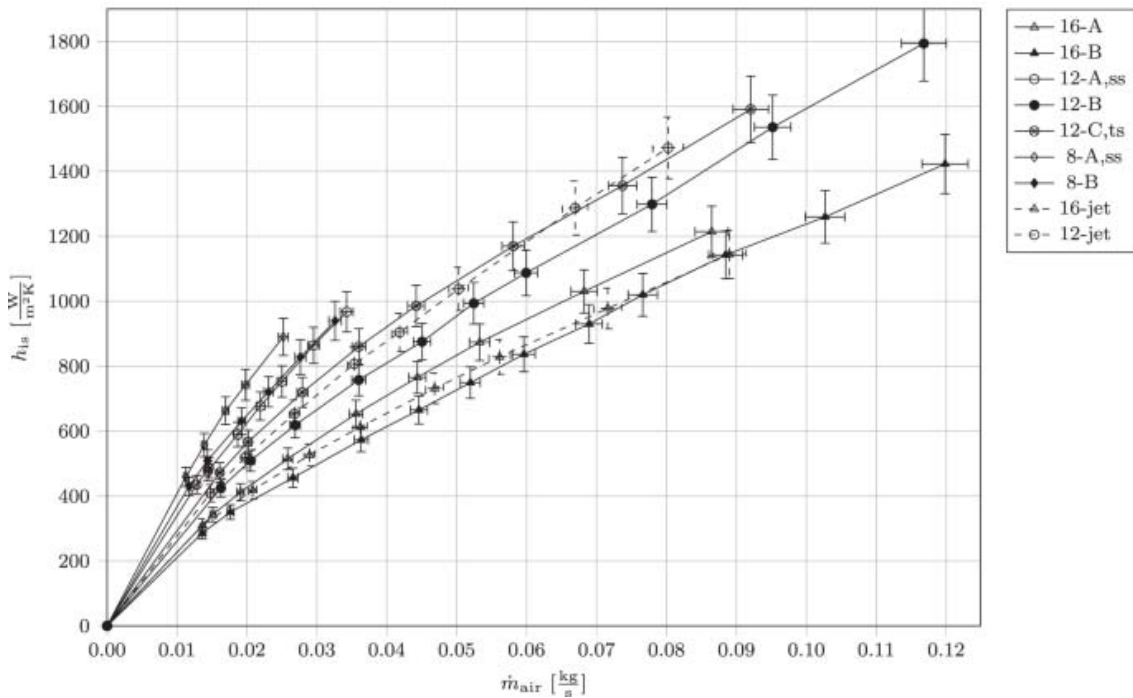
Fig. 10. Experimental overall heat transfer coefficients of the Tadpole configurations compared with the conventional impinging jets from [15] along with the maximum sensor uncertainty
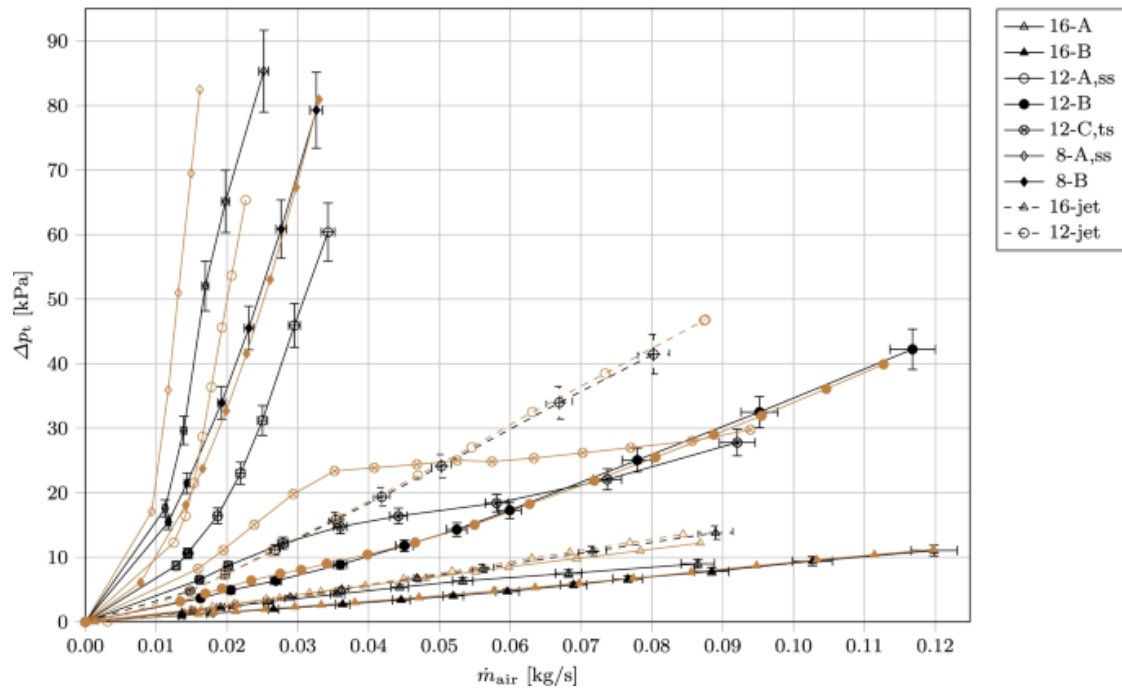
Fig. 11. Experimental total pressure losses over the heated (black) and unheated (brown) domains of the Tadpole configurations compared with the impinging jets from [15] along with the maximum sensor uncertainty
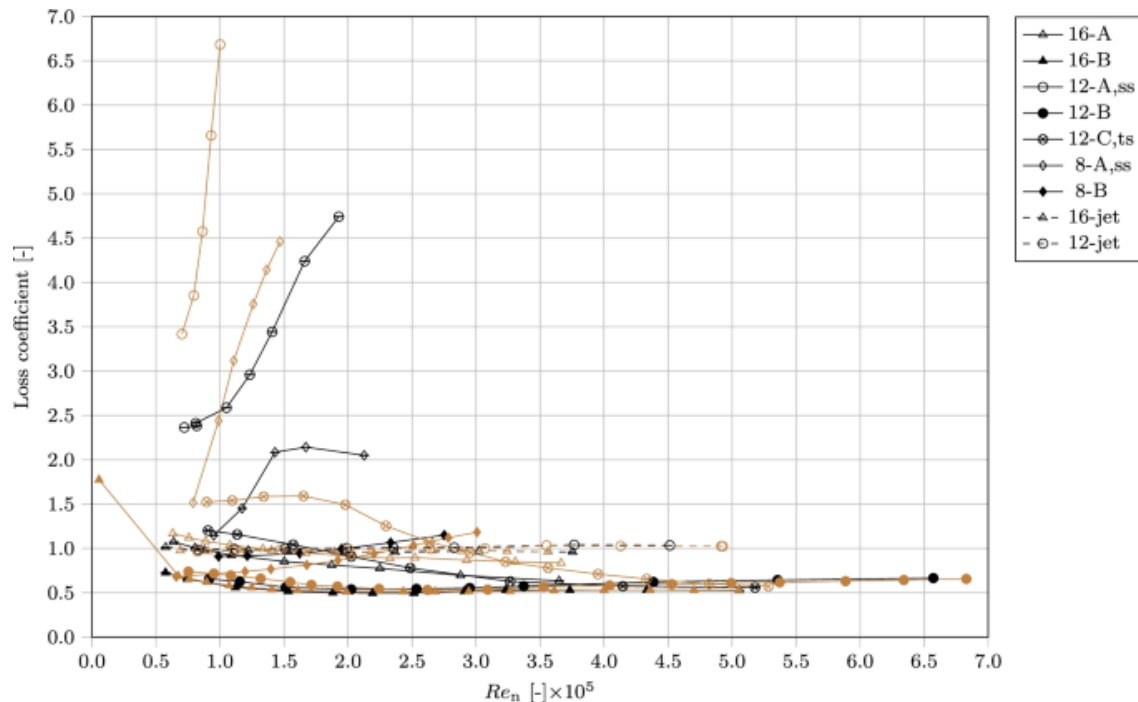
Fig. 12. Experimental loss coefficients (based on the dynamic pressure at the nozzle region) of the Tadpole configurations compared with the impinging jets from [15] for the heated domain (black) and the unheated domain (brown)

It is observed that, in an experimental Tadpole configuration where the peak flow velocity substantially exceeds that of a corresponding impinging jet, the heat transfer coefficient is

greater; but where the peak velocity is the same or even slightly higher, the heat transfer coefficient is lower. From the CFD model described in Sect. 5, it is observed that the impinging jet characteristically maintains the maximum developed velocity around the impingement surface (after being redirected by the surface) for a longer arc length than a corresponding Tadpole. After impingement, the flow of the impinging jet is constrained only by the impingement surface, whereas the Tadpole constrains the flow with two walls (in the narrow flow region). Immediately downstream of the Tadpole's nose, the narrow flow region (of the experimental prototypes) decelerates the flow. The impinging jet domain does not exhibit deceleration in the wall jet at the same rate due to less constraint on the flow movement near the heat transfer surface. The impinging jet also generates significantly higher turbulence kinetic energy levels near the velocity gradient (mixing layer) of the wall jet whereas the Tadpole does not generate high levels of turbulence kinetic energy due to the absence of a mixing layer.

It is accordingly postulated that the increased deceleration of a similar peak velocity magnitude and significantly reduced turbulence kinetic energy within the narrow flow region of the Tadpole (relative to an impinging jet with a similar peak velocity magnitude) results in an increased boundary layer thickness, thereby developing a lower surface heat transfer coefficient. This may be improved in the future with a non-hemispherical Tadpole surface to maintain the peak velocity magnitude through the narrow flow region.

7.1.2 Total pressure loss characteristics

The total pressure losses are presented in Fig. 11 for the heated and unheated (ambient temperature) domains. The two result-sets with the steepest gradients correspond with the supersonic cases and the sets with the most gradual gradients correspond with configurations developing the lowest peak velocity magnitude. It is demonstrated that both the heat transfer coefficient and total pressure loss increase with the peak velocity magnitude.

Comparing performance characteristics between the Tadpoles and the jets, it is shown that 16-A experiences a 13% lower (average) total pressure loss (in the heated domain) compared with 16-jet while the heat transfer coefficient is higher for all mass flow rates by an average of 7.3%. The 12-C,ts case experiences significantly lower pressure losses than 12-jet at higher mass flow rates while the heat transfer coefficients are similar; the averaged improvement for this comparison is a 3.2% increase in h_{is} with a reduction in Δp_t of 14%. This demonstrates that the Tadpole is capable of outperforming an impinging jet.

The loss coefficients for the heated and unheated domains are presented in Fig. 12. The jet configurations produce a loss coefficient of around 1 for the turbulent flow regime indicating that all the dynamic pressure developed in the nozzle is dissipated.

Several subsonic Tadpole configurations produce loss coefficients of less than 1, indicating that the narrow flow region and the diffuser are able to substantially recover the dynamic pressure developed in the nozzle region (even after a further increase in dynamic pressure downstream of this region towards the Tadpole's nose). Of the prototype configurations, 16-B reaches the smallest (ambient temperature) loss coefficient of 0.512. The supersonic

loss coefficients are more than 1 because the narrow flow region is significantly accelerating the flow velocity (and thereby the dynamic pressure) downstream of the Tadpole's nose. This indicates that a supersonic Tadpole is unfavourable. In summary, the Tadpole shows favourable performance in the subsonic realm and the turbulent flow regime.

The results show that the impinging jet loss coefficient demonstrates independence to the Reynolds number within the turbulent flow regime. A characteristic difference can be observed when comparing the jet configurations and the Tadpoles. The Tadpole configurations produce loss coefficients that change with Reynolds number while it is expected that subsonic loss coefficients for a fixed geometry should remain constant (as with the jets) in the turbulent flow regime — turbulent Reynolds number independence was also shown for diffuser performance metrics in Adkins et al. [17].

It is thus understood that the variation in loss coefficient within the turbulent flow regime for the subsonic Tadpole configurations can be attributed only to the shifting of ξ with mass flow rate (described in Sect. 4.3.7). One similarity with the jets is that the loss coefficients for the configurations with a lower peak velocity: 16-A and 16-B tend to be slightly higher at lower Reynolds numbers, this region is understood to be a laminar to turbulent transition. In support of this, [16] shows that laminar boundary layers separate more readily under an adverse pressure gradient and that such a separation affects diffuser performance adversely. For the example of the 16-B case, the first ambient-temperature data-point has a significantly higher loss coefficient, this could be due to flow separation in the narrow flow region or in the diffuser caused by laminar or transitional flow.

The experimental results have been presented and the Tadpole has demonstrated promising performance in comparison to the conventional impinging jet. The proceeding section uses the experimental results to validate a CFD model.
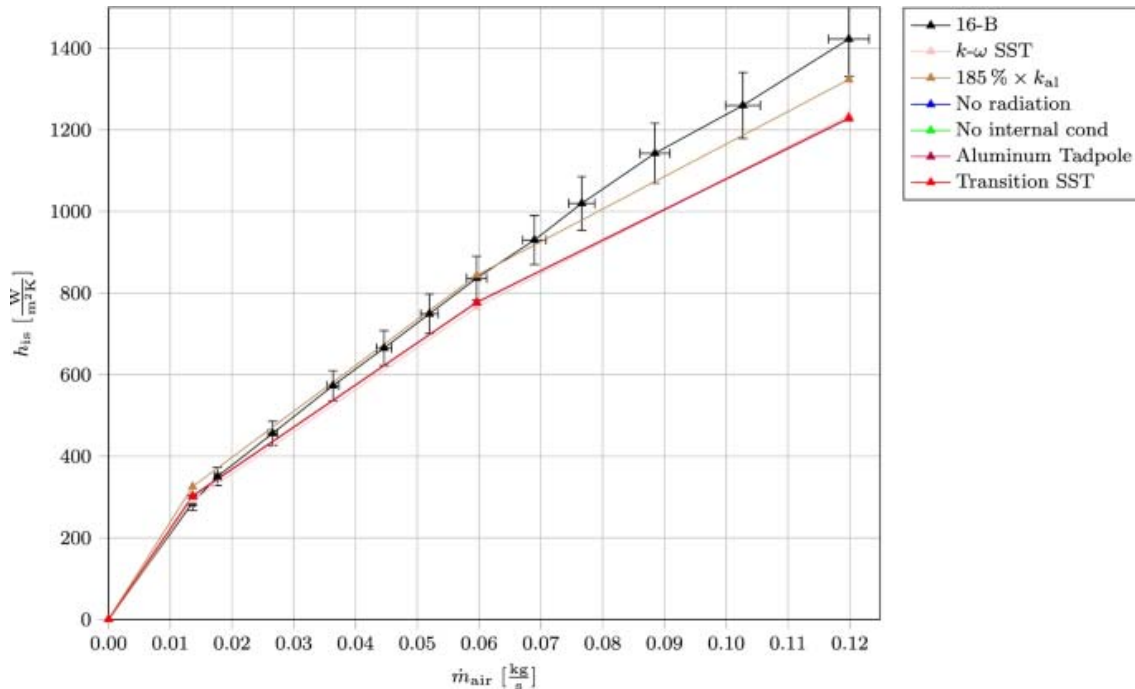
7.2 CFD results

This section firstly presents an initial CFD validation sensitivity of this domain and secondly a full validation with the most suitable turbulence model. Thereafter, additional insights are gleaned from the CFD model.

7.2.1 Validation sensitivity

An example Tadpole and impinging jet configuration were chosen for an extensive turbulence validation and modelling sensitivity study. A turbulence model comparison is given in Table 6. It is demonstrated that the same Four-Equation Transition SST turbulence model previously validated for the impinging jet [15] shows better validation for this Tadpole configuration in comparison to the k-ω SST model. This was also observed for the other subsonic and transonic Tadpole configurations.

Fig. 13. Experimental (black) overall heat transfer coefficients of the 16-B Tadpole configuration and CFD results (colour) of various domain and model modifications; with the bottom four legend entries varying only slightly

Table 6. Average deviation between the CFD turbulence models and the experimental results

	16-B		16-jet [15]	
	k-ω SST	Transition SST	k-ω SST	Transition SST
h_{is}	−6.59%	−4.88%	11.9%	5.12%
Δp_t	−35.4%	−33.4%	−4.72%	−6.93%

To investigate parameters that affect the heat transfer validation, the model's sensitivity to various effects is shown in Fig. 13. Included are the turbulence model, the conductivity of the aluminium outer shell, the deactivation of internal conduction through the plastic Tadpole part and aluminium nozzle, internal radiation as well as a hypothetical aluminium Tadpole (to determine whether conduction through the Tadpole is favourable). The latter effects were investigated with the Transition SST turbulence model.

Figure 13 shows that for the low temperature experimental setup: internal radiation makes almost no difference to the low temperature heat transfer characteristics. Although, the radiation effects are more significant at higher temperatures — such as in the application of a solar thermal receiver.

Figure 13 demonstrates a negligible heat transfer effect of deactivating internal conduction through the Tadpole. Furthermore, it is demonstrated that a hypothetical aluminium Tadpole also has almost no heat transfer effect [2]. This confirms the initial expectation that conduction through the Tadpole is not necessarily favourable.

The most notable effect in Fig. 13 is increasing the thermal conductivity of the aluminium alloy to that of pure aluminium (185%×k_{al}). This is attributed to conjugate heat transfer occurring in the domain. Moreover, the system is highly sensitive to the conductivity of the outer shell and the flange because, with an elevated k_{al}, the condensation heat flux travels farther through the flange and the annular outer shell, thereby increasing the effective interior convective heat transfer area and amplifying the observed heat transfer coefficient.

7.2.2 Validation results

The experimental results are compared with the Four-Equation Transition SST CFD model in Figs. 14 and 15. Two corresponding impinging jet validation sets from Erasmus et al. [15] are also shown in the figures with the same turbulence model and settings. The subsonic and transonic Tadpole configurations deviate by an average (absolute value deviation) of 4.60% in h_{is} and 27.8% in Δp_t from the CFD results excluding four outliers with Δp_t deviations larger than 50%.
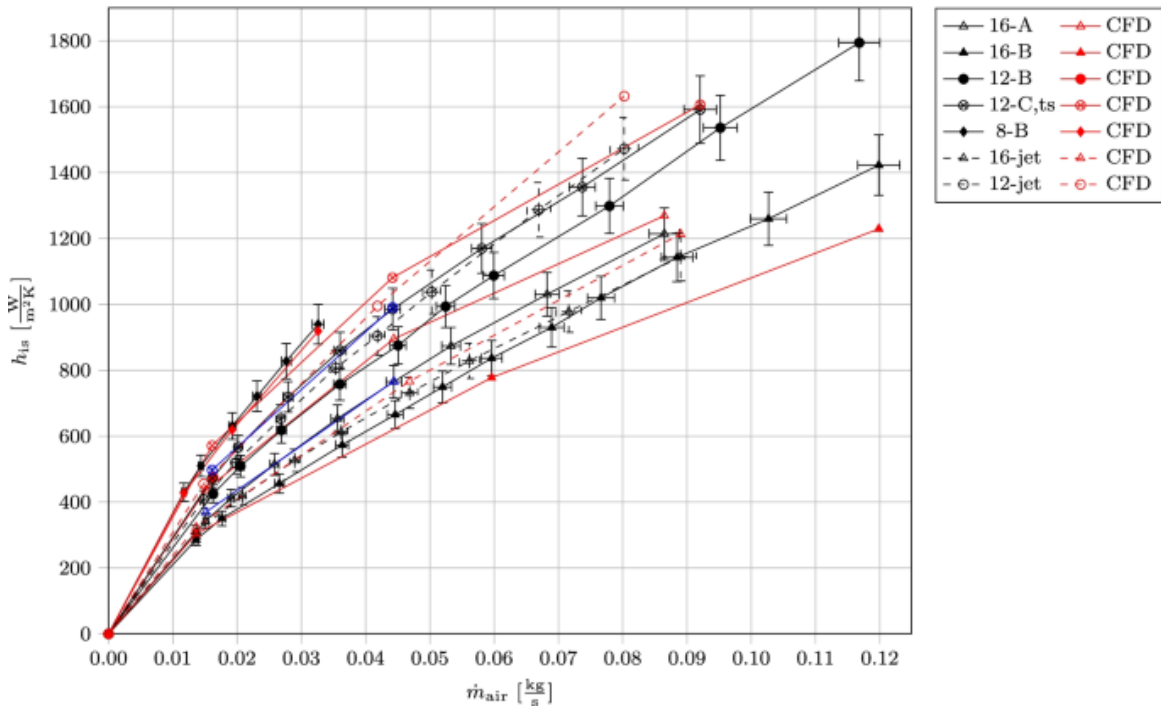
Fig. 14. Experimental (black) and default CFD (red) overall heat transfer coefficients of the Tadpoles compared with the impinging jets from [15] as well as the corrected ξ CFD results (blue)
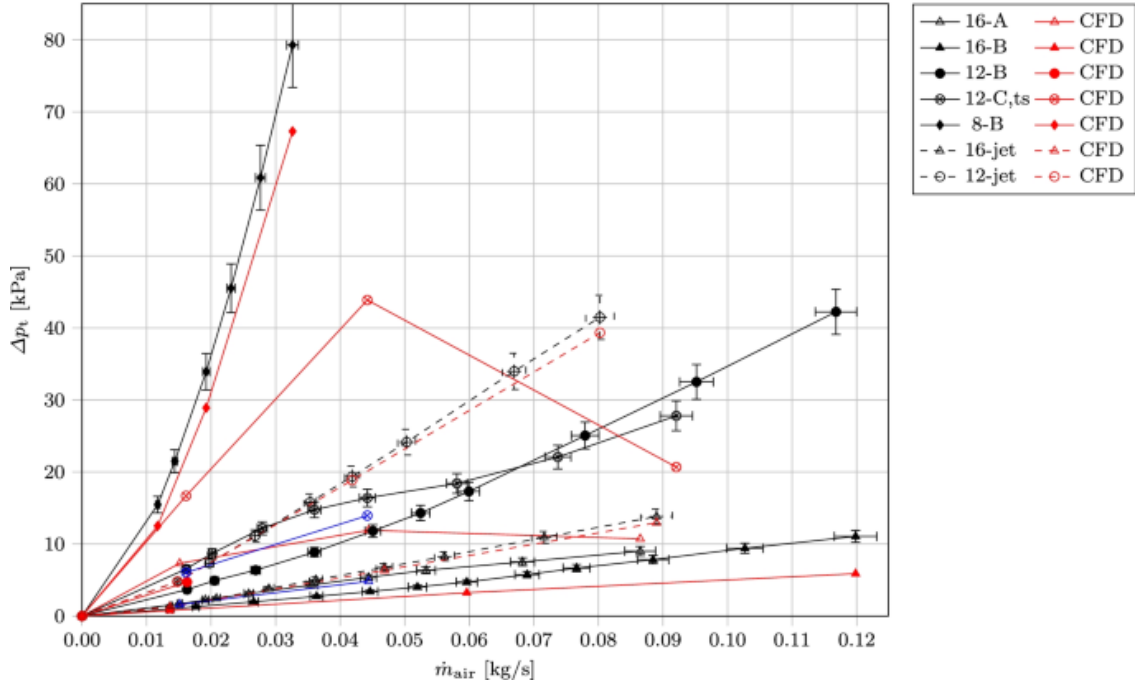
Fig. 15. Experimental (black) and default CFD (red) total pressure losses of the Tadpoles compared with the impinging jets from [15] as well as the corrected ξ CFD results (blue)

From Sect. 6.2, a dominating uncertainty was expected from the measurement of ξ for the domain. This is understood to be the cause of four outlier data-points as well as the inconsistency in the deviations between configurations. Accordingly, a further analysis on ξ was conducted on the CFD mesh for these outliers to correct the predictions of ξ. Moreover, the ξ value in the CFD mesh of the outliers was modified until the resulting CFD $h$is became similar to that of the experimental results — these are represented in blue in the validation figures. The average modification on ξ was −0.42mm (near the 0.5 mm discretization interval of the ξ measurement device. The result is that the corrected data-points deviate significantly less than before and to a similar degree of the impinging jets' deviations. It is clear that a small change in ξ can affect the performance characteristics significantly. This is a limitation of the current design.

Including the corrected results, the CFD validation deviation becomes 4.29% for h_{is} and 22.9% for Δp_t. The impinging jets demonstrate substantially better validation of 6.88% for $h$is and 7.71% for Δp_t with the same turbulence model. Because it was shown that the increased deviation of only the Tadpole's CFD validation cases is attributed to the uncertainty in ξ, the CFD model is deemed satisfactorily validated.

7.2.3 Flow domain illustrations

Total pressure, Mach number and static temperature contours are presented in Fig. 16. The temperature contours show the heating of the flow along with a thermal boundary layer development in the adverse pressure gradient of the narrow flow region. The conjugate heat transfer characteristics are shown visually: the condensation heat flux conducts through the hemisphere, the flange and the annulus (to a lesser degree) to reach the convection domain.
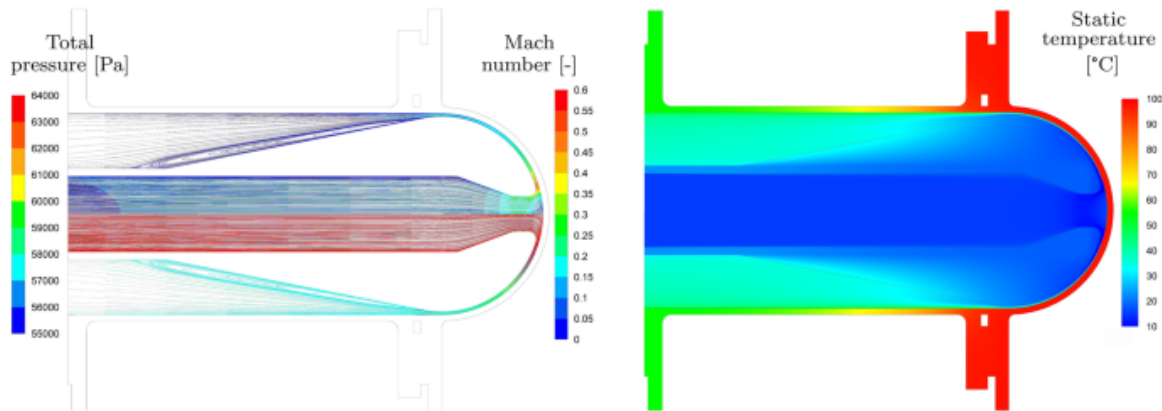
Fig. 16. CFD pathlines showing the Mach number (left, top) and the total pressure (left, bottom) contours as well as the static temperature contours (right) for the 12-C,ts Tadpole at 'state 1' (the boundary conditions are given in Table 4)

The characteristic total pressure and Mach number contours of a Tadpole configuration demonstrates that most of the total pressure losses occur in the adverse pressure gradient region, particularly the narrow flow region, where the sharpest reduction of Mach number occurs. Because the change in total pressure is significantly sharper where the Mach number decreases instead of where the Mach number is highest near the walls, it is understood that, as with an impinging jet [15], skin friction plays a less important role in comparison with expansion losses in the Tadpole's domain of this investigation. This indicates that there is still room for improvement in the narrow flow region to reduce the rate of expansion with a non-hemispherical Tadpole surface such as a revolved spline. Reducing the rate of expansion here is expected to reduce the growth rate of the boundary layer and thereby should increase the heat transfer performance.

The total pressure pathlines also depict a narrow vortex occurring in the diffuser, thereby suggesting that a smaller expansion angle (and thus an increased diffuser length) may improve the domain. As described in Sect. 4.3.1, the maximum diffuser length was constrained in the experimental setup.

8 Conclusion

The novel Tadpole concept has been presented as an impingement heat transfer device with improved pressure recovery to improve the flow domain of the conventional impinging jet.

Multiple dimensional degrees of freedom in the Tadpole's flow domain can be manipulated for an enhanced heat transfer coefficient, a reduced total pressure loss or a favourable combination of both metrics. The experimental results show that two Tadpole configurations (16-A and 12-C,ts) are capable of outperforming a conventional impinging jet as a heat transfer device. The 16-A configuration demonstrates a 7.3% increase in h_{is} with a 13% decrease in Δp_t and the 12-C,ts configuration demonstrates a 3.2% increase in h_{is} with a 14% decrease in Δp_t when compared with corresponding impinging jet configurations. The Tadpole therefore shows favourable performance in the subsonic realm and the turbulent flow regime.

A CFD model based on the Four-Equation Transition SST turbulence model was developed and compared with the experimental results. The average (absolute) deviation between the model and the experimental results is 4.29% for h_{is} and 22.9% for Δp_t after four outliers were corrected — the same model previously validated for the impinging jet's flow domain demonstrates satisfactory validation for the Tadpole's flow domain. It was found that the greatest sensitivities to the CFD validation (besides the turbulence model) is the Tadpole's axial position (ξ) and the aluminium conductivity (k_{al}).

The sensitivity of the Tadpole to its axial position is a limitation of the current design. To mitigate this in future manifestations: the measurement accuracy and stiffness of the axial position should be improved; alternatively, the Tadpole can be dimensionally up-scaled to mitigate the effect of the axial-position-measurement uncertainty.

The CFD results indicate that the performance of the Tadpole may be improved with a non-hemispherical Tadpole surface such as a revolved spline to constrain a near constant flow velocity in the narrow flow region. This is expected to reduce the rate of flow expansion and also reduce the growth rate of the boundary layer and thereby should increase the heat transfer coefficient and decrease the total pressure loss.

9 Further work

It is recommended that the inherent potential in the multiple-degree, design space freedom of the Tadpole's domain be explored with an optimisation study. To constrain a near constant velocity in the narrow flow region for potentially improved performance, a non-hemispherical Tadpole surface should also be investigated.

Further work is also recommended to explore the incorporation of fins within the diffuser region, as depicted in Fig. 4.

Availability of data and material

Further data can be made available on request.

Acknowledgements

Funding

Contributions

Derwalt J. Erasmus: Investigation, Matti Lubkoll: Supervision, Ken J. Craig: Supervision, Theodor W. von Backström: Supervision.

Notes

1. The turbulence intensity was not investigated experimentally. Instead, it was approximated using fully developed turbulent duct flow empirical correlations from [32].
2. The incremental effects can be observed by zooming into Fig. 13.

References

1. Goldstein R, Behbahani A, Heppelmann K (1986) Streamwise distribution of the recovery factor and the local heat transfer coefficient to an impinging circular air jet. Int J Heat Mass Transf 29(8):1227–1235. https://doi.org/10.1016/0017-9310(86)90155-9
2. Achari AM, Das MK (2015) Application of various RANS based models towards predicting turbulent slot jet impingement. Int J Therm Sci 98:332–351. https://doi.org/10.1016/j.ijthermalsci.2015.07.018
3. Fabbri M, Jiang S, Dhir VK (2003) Experimental investigation of single-phase micro jets impingement cooling for electronic applications. In: Proceedings of the ASME 2003 Heat Transfer Summer Conference. Heat Transfer: Volume 3, ASMEDC, Las Vegas, https://doi.org/10.1115/HT2003-47162
4. Garbrecht O, Al-sibai F, Kneer R, Wieghardt K (2012) Numerical Investigation of a New Molten Salt Central Receiver Design. In: SolarPACES 2012, Marrakech
5. Wang W, Laumert B (2018) An axial type impinging receiver. Energy 162:318–334. https://doi.org/10.1016/j.energy.2018.08.036
6. Lubkoll M, Erasmus DJ, Harms TM, Von Backström TW, Kröger DG (2020) Performance characteristics of the spiky central receiver air pre-heater (SCRAP). Sol Energy 201:773–786. https://doi.org/10.1016/j.solener.2020.03.027
7. Quick J (2020) Computational investigation of swirling jet impingement in a concentrated solar tower cavity receiver. Master's thesis, University of Pretoria, South Africa
8. Kobayashi T, Banno M, Amaoka K (2000) Leading edge structure of aircraft airfoil and method of fabricating the same. https://patents.google.com/patent/US6119978
9. Brand JH, Dowhan MJ (2009) Anti-icing apparatus and method for aero-engine nose cone. https://patents.google.com/patent/US20090120099A1
10. Bunker RS, Metzger DE (1990) Local Heat Transfer in Internally Cooled Turbine Airfoil Leading Edge Regions: Part I - Impingement Cooling Without Film Coolant Extraction. J Turbomach 112(3):451–458. https://doi.org/10.1115/1.2927680
11. Zamma J, Nishimura Y, Nakajima Y, Sakai T (1984) Bayonet tube heat exchanger. Patent. https://patents.google.com/patent/US4431049A/en
12. Alzoubi MA, Sasmito AP (2017) Thermal performance optimization of a bayonet tube heat exchanger. Appl Therm Eng 111:232–247. https://doi.org/10.1016/j.applthermaleng.2016.09.052

13. Ma T, Zeng M, Ji Y, Zhu H, Wang Q (2011) Investigation of a novel bayonet tube high temperature heat exchanger with inner and outer fins. Int J Hydrogen Energy 36(5):3757–3768. https://doi.org/10.1016/j.ijhydene.2010.12.039

14. Damiani L, Montecucco M, Prato AP (2013) Conceptual design of a bayonet-tube steam generator for the ALFRED lead-cooled reactor. Nucl Eng Des 265:154–163. https://doi.org/10.1016/j.nucengdes.2013.06.021

15. Erasmus DJ, Lubkoll M, Von Backström TW (2020) Jet impingement heat transfer within a hemisphere. Heat Mass Transf. https://doi.org/10.1007/s00231-020-02977-9

16. Çengel YA, Cymbala JM (2014) Fluid Mechanics Fundamentals and Applications, 3rd edn. McGraw-Hill, New York

17. Adkins RC, Jacobsen OH, Chevalier P (1983) A preliminary study of annular diffusers with constant diameter outer walls (suitable for turbine exits). The American Society of Mechanical Enigneers 1(83-GT-218), https://doi.org/10.1115/83-GT-218

18. Erasmus DJ, Von Backström TW, McDougall D, Lubkoll M (2019) Heat transfer device, PCT international patent application. PCT/IB2019/060650

19. Bekker GM, Meyer CJ, Van der Spuy SJ (2020) Numerical investigation of pressure recovery for an induced draught fan arrangement. R&D J South African Inst Mech Eng 36:19–28, http://dx.doi.org/10.17159/2309-8988/2020/v36a3

20. Herschel C (1888) Apparatus for measuring the quantity of water flowing through a pipe. https://pdfpiw.uspto.gov/.piw?PageNum=0&docid=00381373&IDKey=&HomeUrl=/

21. Kröger DG (2008) Spiky Central Receiver Air Pre-heater (SCRAP). Stellenbosch University, Tech Rep

22. Viereckl F, Schleicher E, Schuster C, Lippmann W, Hurtado A (2019) Experimental and theoretical investigation of the boiling heat transfer in a low-pressure natural circulation system. Experimental and Computational Multiphase Flow 1(4):286–299. https://doi.org/10.1007/s42757-019-0023-0

23. VDI (2010) VDI-Wärmeatlas, 10th edn. Springer-Verlag, Berlin Heidelberg, Germany

24. Eucken A (1940) Allgemeine Gesetzmäßigkeiten für das Wärmeleitvermögen verschiedener Stoffarten und Aggregatzustände. Forschung auf dem Gebiet des Ingenieurwesens A 11(1):6–20. https://doi.org/10.1007/BF02584103

25. MatWeb (2019) Overview of materials for acrylonitrile butadiene styrene (ABS), molded. http://www.matweb.com/search/datasheet_print.aspx?matguid=eb7a78f5948d481c9493a67f0d089646&n=1

26. Mikron Instrument Company (2003) Table of emissivity of various surfaces. Mikron Instrument Company Inc, USA

27. Fives North American Combustion I (2001) North American Combustion Handbook, 3rd edn. page 85, Fives North American Combustion, Inc., USA, https://app.knovel.com/hotlink/toc/id:kpCHVIE001/north-american-combustion/north-american-combustion

28. Erasmus D (2020) The development of a novel impingement heat transfer device. Master's thesis, Stellenbosch University, South Africa, https://scholar.sun.ac.za/handle/10019.1/109296

29. Kröger DG (2004) Air-cooled Heat Exchangers and Cooling Towers, 1st edn. Stellenbosch University, South Africa

30. Johnston IH (1953) The effect of inlet conditions on the flow in annular diffusers. Memorandum M.167, National Gas Turbine Establishment
31. Launder B, Spalding D (1983) Paper 8 - The Numerical Computation of Turbulent Flows. In: Patankar SV, Pollard A, Singhal AK, Vanka SP (eds) Numerical Prediction of Flow, Heat Transfer, Turbulence and Combustion, Pergamon, pp 96 – 116, https://doi.org/10.1016/B978-0-08-030937-8.50016-7
32. ANSYS (2016) Fluent theory guide. in: ANSYS documentation. Tech. Rep. 17, ANSYS
33. Bredberg J (2000) On the wall boundary condition for turbulence models. Department of Thermo and Fluid Dynamics, Chalmers University of Technology, Tech. rep.
34. McDougall D (2019) Numerical simulation of jet impingement cooling of the inside of a hemisphere with application to SCRAP. Master's thesis, Stellenbosch University, South Africa, http://hdl.handle.net/10019.1/106154

35. Menter FR (1993) Zonal two equation k-ω turbulence models for aerodynamic flows. AIAA Paper 93-2906 https://ntrs.nasa.gov/search.jsp?R=19960044572
36. Lee DH, Chung YS, Won SY (1999) The effect of concave surface curvature on heat transfer from a fully developed round impinging jet. Int J Heat Mass Transf 42(13):2489–2497. https://doi.org/10.1016/S0017-9310(98)00318-4
37. Langtry RB, Menter FR (2009) Correlation-based transition modeling for unstructured parallelized computational fluid dynamics codes. AIAA J 47(12):2894–2906. https://doi.org/10.2514/1.42362
38. Craig KJ, Slootweg M, Meyer JP (2018) Heat transfer enhancement in molten salt central receiver using jet impingement. In: 5th Southern African Solar Energy Conference (SASEC), Durban, South Africa., vol 5, https://www.sasec.org.za/full_papers/53.pdf
39. Zuckerman N, Lior N (2006) Jet Impingement Heat Transfer: Physics, Correlations, and Numerical Modeling. Advances in Heat Transfer 39(C):565–631, https://doi.org/10.1016/S0065-2717(06)39006-5
40. Schobeiri MT (2010) Fluid Mechanics for Engineers. Springer, Berlin Heidelberg, Germany
41. Taylor J (1997) An introduction to error analysis: The study of uncertainties in physical measurement, 2nd edn. University Science Books, USA